AIAA-2005-0089

43rd AIAA Aerospace Sciences Meeting and Exhibit, January 10-13 2005, Reno NV

Progress Towards Computational Method for Circulation Control Airfoils

R. C. Swanson*, C. L. Rumsey†, S. G. Anders‡

NASA Langley Research Center, Hampton, VA 23681-2199, USA

Abstract

The compressible Reynolds-averaged Navier-Stokes equations are solved for circulation control airfoil flows. Numerical solutions are computed with both structured and unstructured grid solvers. Several turbulence models are considered, including the Spalart-Allmaras model with and without curvature corrections, the shear stress transport model of Menter, and the k-enstrophy model. Circulation control flows with jet momentum coefficients of 0.03, 0.10, and 0.226 are considered. Comparisons are made between computed and expermental pressure distributions, velocity profiles, Reynolds stress profiles, and streamline patterns. Including curvature effects yields the closest agreement with the measured data.

Introduction

Flow control offers a multitude of opportunities to improve not only aerodynamic performance but also safety and environmental impact of flight vehicles.[1] Circulation control (CC) is one type of flow control that is currently receiving considerable attention. Such flow control is usually implemented by tangentially injecting a jet sheet over a rounded wing trailing edge. The jet sheet remains attached farther along the curved surface of the wing due to the Coanda effect (i.e., a balance of the pressure and centrifugal forces). This results in the effective camber of the wing being increased, which produces lift augmentation. A CC configuration offers the possibility of reduced take-off and landing speeds as well as increased maneuverability. Further, the use of pulsed jets with CC systems, as discussed by Jones and Englar,[2] provides the possibility of significantly reducing the mass flow required to achieve a desired performance, a principal obstacle to the installation of CC systems on production aircraft.

Computational methods will play a vital role in designing effective CC configurations. Certainly, detailed experimental data, such as velocity profiles and Reynolds stresses, will be absolutely essential for validating these prediction tools. Due to the cost of flow control experiments, design and parametric studies will strongly depend on accurate and efficient prediction methods. These methods must have the potential to treat pulsating jets, even multiple jets, for a broad range of flow conditions (e.g., Mach number, Reynolds number, angle of attack). In general, the numerical methods must be extendable to time-dependent and three-dimensional flows.

At the circulation control workshop[3] held at NASA Langley in 2004, an effort was made to assess the current capability to calculate CC airfoil flows. Although the assessment included a wide range of applications, the focus was the computation of the flow over the CC airfoil configuration (NCCR 1510-7067) tested by Abramson.[4] Various computational methods and a variety of turbulence models, ranging from

*Senior Research Scientist, Computational Modeling and Simulation Branch, Mail Stop 128, Senior Member AIAA.

†Senior Research Scientist, Computational Modeling and Simulation Branch, Mail Stop 128, Associate Fellow AIAA.

‡Research Engineer, Flow Physics and Control Branch, Mail Stop 170.

an algebraic model to a full Reynolds stress model, were considered. Predicted pressure distributions were compared with experimental pressure data. The range of numerical solutions presented underscored the importance of turbulence modeling in predicting such complex turbulent flows. In addition, different results were frequently obtained with the same turbulence model. The need to clearly identify the version of a given turbulence model being used was evident, especially since relatively simple changes in a model can have a dramatic impact on the flow solution.

In a paper[5] presented at the workshop we applied the compressible Navier-Stokes solver CFL3D[6] in computing the flow over the CC airfoil geometry in the experiment of Abramson and Rogers.[7] This airfoil geometry very closely approximates that of the Abramson[4] experiment. Calculations were performed for the two low Mach number ($M = 0.12$) cases of the workshop, having angles of attack equal to zero and -8 degrees, as well as for a $M = 0.6$ case. With the Spalart-Allmaras (SA) turbulence model that includes curvature effects,[8] which is designated the SARC model, and the 1994 version of the shear stress transport (SST) model of Menter[21] reasonably good agreement was obtained with the measured pressure data for the low Mach number cases. An unusually large value of the curvature correction parameter seemed to be necessary for the SARC model. The SST model exhibited sensitivity to changes in the modeling of the turbulence production term. For the $M = 0.6$ case the surface pressures computed with this model compared poorly with the data. There was a clear need for further investigation of these turbulence models as well as others. For such additional study detailed experimental data was considered of paramount importance not only for examining the effects of turbulence modeling but also for validating the accuracy of the computational method.

With the purpose of providing data for Navier-Stokes validation, Novak et al[10] used two-dimensional laser doppler velocimetry to obtain detailed flow-field data for the low speed flow over a 15.6 percent thick CC airfoil geometry with a supercritical leading edge and circular trailing edge. Extensive flow-field surveys, including velocity and Reynolds stress profiles were taken on the aft section of the airfoil for two values of the jet momentum coefficient. Previously, Shrewsbury[12,13] and Viegas et al.[14] solved the compressible Reynolds-averaged Navier-Stokes equations and made comparisons primarily with experimental pressure data and streamlines. By varying the angle of attack for the computations until the experimental lift coefficient was matched, Shrewsbury obtained computed pressures that compared well with the measured pressure data. In these calculations the mixing length of the algebraic eddy viscosity model of Baldwin and Lomax[15] was modified by an empirical curvature correction.

Viegas et al. attempted to eliminate some of the uncertainties associated with wind tunnel wall corrections by including lower and upper tunnel walls in simulating the Navak et al. experiment. Several versions, with and without curvature corrections, of the Baldwin-Lomax and the two-equation Jones-Launder models were considered. This approach did not account for the important interference effects produced by the tunnel sidewalls. Thus, there were significant differences between computed and experimental pressure distributions on the suction surface of the airfoil.

In the current work we make detailed comparisons of numerical solutions with the extensive flow-field measurements of the Novak et al. experiment. The purpose of the work is not only to assess the numerical prediction capability of the CFD codes for CC airfoil flows but also to examine the effects of turbulence modeling on the flow field. The SA, SARC, SST, and k-enstrophy transport equation models are considered. Comparisons are made between computed and experimental pressures, velocity and Reynolds stress profiles, and streamline patterns. The effect of streamline curvature is demonstrated by comparing results computed with the SA and SARC models. Preliminary results for a three-dimensional simulation of the CC wing model in the wind tunnel are presented.

The initial sections of the paper concern the CC airfoil geometry and flow conditions, description of grids, numerical method, and boundary conditions. This is followed by a section on turbulence modeling, where emphasis is given to the implementation details of the models that can significantly affect their performance. In the final sections the numerical results are discussed and concluding remarks are given.

C_μ	α_{cor}(deg)
0.030	-2.46
0.100	-5.86
0.226	-8.94

Table 1. Angle of attack correction.

Geometry and Flow Conditions

The circulation control wing (CCW) model in the Novak et al. experiment has a chord of 15 inches and a span of 24 inches, resulting in an aspect ratio of 1.6. The CC airfoil section has a supercritical leading edge, symmetric middle section and a 2 inch diameter Coanda CC aft section. It has a thickness ratio of 15.6 percent. The jet slot height-to-chord ratio is 0.002, which corresponds to a slot height of 0.03 inches.

For the tests conducted by Novak et al. the free-stream Mach number is 0.12 and the Reynolds number is 0.986×10^6. The geometric angle of attack is zero degrees. The values of the jet momentum coefficient (C_μ), which is the ratio of the jet momentum to the free-stream momentum, for which laser doppler velocimeter (LDV) data were taken on the Coanda surface are 0.03 and 0.10.

Although the experiment is designed to be two-dimensional, there are three-dimensional effects due to the presence of the sidewalls in the wind tunnel. The interaction of the sidewall boundary layers with the wing and its Coanda surface produce vortical structures that induce a downwash along the span of the wing, reducing the effective angle of attack. For the C_μ values being considered in this paper the angle of attack corrections suggested by the experimenters are given in Table 1. All two-dimensional computations presented in this paper employ these corrections.

Computational Grids

For the two-dimensional numerical computations both structured and unstructured grids were considered. Both grids have similar normal spacing for resolving the viscous layer near walls. However, the structured grid is only weakly clustered in the direction normal to the blunt trailing edge (thickness of 0.024 inches) of the lip of the jet slot. Thus the viscous layer on this edge is not resolved, and the recirculation region occurring there is not captured. In order to determine the influence of the resolution of this lip edge, calculations were performed on an unstructured grid with strong clustering at the lip edge. For both types of grids the domain surrounding the CC airfoil extended 40 chords away from the airfoil.

In the case of the structured grid the discretized domain was partitioned with three blocks. At the interface boundary on the lower airfoil surface the grid is patched, as seen in Fig. 1a, which displays the near field of the fine resolution grid. This grid includes 577 grid points around the airfoil and 145 points in the normal direction over the forward part of the airfoil. Over the aft part of the airfoil there are 241 points in the normal direction, and this number includes the points in the plenum for the jet. Including the plenum the fine grid contains 114,336 points. The grid is tangentially clustered at the airfoil leading edge. In the normal direction the grid spacing at the wall is 4×10^{-6} yielding an average normalized coordinate y^+ that is less than one for the first grid cell at the wall. The quantity y^+ is defined by $y\sqrt{\tau_w/\rho}/\nu$, where τ_w is the shear stress at the wall, ρ is density, and ν is the kinematic viscosity. For the medium grid the number of cells in the fine grid is halved in each coordinate direction.

For the three-dimensional simulation of the CCW configuration in the wind tunnel, the structured grid contains 33 spanwise planes. The grid in the spanwise direction was constructed by distributing planes of the two-dimensional grid from the tunnel sidewall to the mid-span location. In order to resolve the sidewall boundary layer, there is clustering of the grid at the sidewall.

The unstructured grid consists of 84,599 nodes and 167,274 cells. A near field view of the grid is displayed in Fig. 1b. On the external surface of the airfoil there are 841 points. There are 25 points along the vertical trailing edge of the lip of the jet slot. The minimum normal wall spacing on the airfoil is 4×10^{-6}. This gives a typical y^+ value of less than 0.4 for most of the airfoil and a maximum value of 1.13 that occurs near the jet exit for the $C_\mu = 0.10$ case. The maximum value of y^+ for the $C_\mu = 0.03$ case is 0.75.

Numerical Methods

Numerical solutions on the structured grid were computed with CFL3D, a multi-zone Reynolds-averaged Navier-Stokes (RANS) code developed at NASA Langley.[6] It solves the thin-layer form of the Navier-Stokes equations in each of the (selected) coordinate directions. It can use one-to-one, patched, or overset grids, and employs local time step scaling, grid sequencing, and multigrid to accelerate convergence to steady state. In time-accurate mode, CFL3D has the option to employ dual-time stepping with subiterations and multigrid, and it achieves second-order temporal accuracy.

The code CFL3D is based on a finite-volume method. The convective terms are approximated with third-order upwind-biased spatial differencing, and both the pressure and viscous terms are discretized with second-order central differencing. The discrete scheme is globally second-order spatially accurate. The flux difference-splitting (FDS) method[16] of Roe is employed to obtain fluxes at the cell faces. Advancement in time is accomplished with an implicit approximate factorization method (number of factors determined by number of dimensions).

In CFL3D, the turbulence models are implemented uncoupled from the mean-flow equations. The turbulent transport equations are solved using an implicit approximate factorization approach. The advection terms are discretized with first-order upwind differencing. The production source term is treated explicitly, while the advection, destruction, and diffusion terms are treated implicitly.

The unstructured grid solutions were computed with FUN2D,[17] a code for solving the full RANS equations on a domain with triangular discretization. The FUN2D code uses a node-based algorithm in which the variables are stored at the vertices of the mesh and the equations are solved on nonoverlapping control volumes surrounding each node. Inviscid fluxes are obtained on the faces of each control volume by applying the FDS scheme of Roe. The viscous terms are evaluated with a finite-volume formulation that results in a central difference type approximation.

In applying FUN2D to steady state computations the solution is obtained with an Euler implicit advancement in pseudo-time. For time-dependent computations a second-order backward time differentiation formula is used, and pseudo-time iterations are employed to relax the equations. The linear system of equations resulting from either formulation is solved iteratively with pointwise red-black Gauss-Seidel relaxation. For turbulent flows the eddy viscosity is determined with the SA model, and the associated transport equation is solved in an uncoupled manner.

Boundary and Initial Conditions

Boundary conditions are required at the inflow (internal and external), outflow, and solid surface boundaries. For numerical computations the physical boundary conditions must be supplemented with numerical boundary conditions, which generally involve extrapolation of flow quantities or combinations of them (e.g., Riemann invariants) from the interior of the domain. Discussion of the numerical boundary conditions is given in the user's manual for CFL3D.[6] At the far-field inflow boundary a Riemann invariant, entropy, and flow inclination angle are specified. A Riemann invariant is specified at the far-field outflow boundary. At the upstream wall of the plenum the following conditions are prescribed in the current study: for $C_\mu = 0.03$, $u/a_\infty = 0.00950$; for $C_\mu = 0.10$, $u/a_\infty = 0.01370$; for $C_\mu = 0.226$, $u/a_\infty = 0.01514$. Here a_∞ is the free-stream speed of sound. At the surface boundaries the no-slip and adiabatic wall conditions are specified. Boundary conditions for the various turbulence models considered herein are given in.[6] The initial solution

is either defined by the free-stream conditions or a coarser grid solution.

Turbulence Modeling

In all the CC airfoil flows the computations are performed fully turbulent; several turbulence models are considered. The two principal models are the one-equation Spalart-Allmaras (SA) model[18] and the Spalart-Allmaras rotation/curvature (SARC) model.[8,19] Two other models for turbulence are also used. One is the two-equation shear-stress transport (SST) model of Menter.[9,20,21] The other model is the $k-\zeta$ model,[22] which is a two-equation model for the turbulent kinetic energy and the enstrophy. The enstrophy represents the variance of vorticity. All of these models are linear eddy-viscosity models that make use of the Boussinesq eddy-viscosity hypothesis. The equations describing these four models can be found in their respective references. However, there are certain details concerning the implementation of the SARC and SST models that are given here in order to precisely identify what form of the model is being applied.

The SA model can be written in general form as

$$\frac{D\tilde{\nu}}{Dt} = \mathcal{P} + \mathcal{D}_{diff} + \mathcal{D}_{diss} \tag{1}$$

where $\tilde{\nu} \sim \nu_t$, and $\mathcal{P}$, $\mathcal{D}_{diff}$, and $\mathcal{D}_{diss}$ are the contributions associated with turbulence due to production, diffusion, and dissipation, respectively. The production term is given by

$$\mathcal{P} = c_{b1}[1 - f_{t2}]W\tilde{\nu}. \tag{2}$$

In the SARC model $\mathcal{P}$ is replaced by

$$\mathcal{P}' = c_{b1}[f_{r1} - f_{t2}]W\tilde{\nu}, \tag{3}$$

$$f_{r1} = (1 + c_{r1})\frac{2r^*}{(1 + r^*)}\left[1 - c_{r3}\tan^{-1}(c_{r2}\tilde{r})\right] - c_{r1}, \tag{4}$$

where the function r^* is the ratio of scalar measure of strain rate to the scalar measure of rotation, the function $\tilde{r}$ depends on the Lagrangian derivative of the strain-rate tensor principal axes angle (see[19] for details), and $c_{r1} = 1$, $c_{r2} = 12$, and $c_{r3} = 0.6 - 1.0$. As c_{r3} is increased, the turbulence production will decrease near convex surfaces. In the results for this paper we use $c_{r3} = 1.0$.

The production term $\mathcal{P}_k$ in the turbulent kinetic energy equation of the Menter SST model can be written as

$$\mathcal{P}_k = \tau_{ij}\frac{\partial u_i}{\partial x_j}, \tag{5}$$

where the stress tensor τ_{ij} is defined as

$$\tau_{ij} = \mu_t\left(\frac{\partial u_i}{\partial x_j} + \frac{\partial u_j}{\partial x_i} - \frac{2}{3}\frac{\partial u_k}{\partial x_k}\delta_{ij}\right) - \frac{2}{3}\rho k\delta_{ij}, \tag{6}$$

and μ_t is the turbulent viscosity, the partial derivatives are strain rates, and k is the turbulent kinetic energy. The production term $\mathcal{P}_\omega$ in the ω equation of the SST model is proportional to $\mathcal{P}_k$. Generally, in the computations with the SST model, the incompressible assumption is imposed, and the turbulent kinetic energy contribution is neglected. Thus,

$$\mathcal{P}_k \approx \mu_t\left(\frac{\partial u_i}{\partial x_j} + \frac{\partial u_j}{\partial x_i}\right)\frac{\partial u_i}{\partial x_j} = 2\mu_t S_{ij}S_{ij}, \tag{7}$$

where S_{ij} is the strain-rate tensor, and $S_{ij}S_{ij}$ represents the dot product of two tensors. Note that it is also common as a further approximation to employ the vorticity rather than the strain-rate tensor (see Menter[9]). In the present work we use Eq. (7) for $\mathcal{P}_k$.

The eddy viscosity determined with the SST model is defined as

$$\nu_t = \frac{a_1 k}{max(a_1\omega; \Omega F_2)}, \tag{8}$$

where a_1 is a constant, ω is equal to the ratio of the turbulent dissipation rate to the turbulent kinetic energy, $\Omega = \sqrt{2W_{ij}W_{ij}}$, and F_2 is a blending function.

Numerical Results

The computational methods described in previous sections were applied to three CC airfoil flow cases from the Novak et al. experiment. As indicated previously the Mach number for all cases is 0.12, and the Reynolds number is 0.986×10^6. The jet momentum coefficients for these cases are 0.03, 0.10, and 0.226, and the corresponding effective angles of attack are given in Table 1. For the first two cases there is detailed measured data on the Coanda surface, and comparisons with the velocity and shear stress profiles are made. In all cases the computed and experimental pressures are compared.

In Fig. 2a a comparison of the surface pressure distributions for $C_\mu = 0.03$ computed with the SA, SARC, SST, and $k-\zeta$ is shown. Calculations were performed on the medium grid with CFL3D. The surface pressures computed with the SA and SST models are nearly the same and they are lower on the suction surface than the experimental pressures. As a result the predicted lift coefficient (C_L) is about 28 percent higher than that which occurs in the experiment. Also, with these models somewhat higher pressures occur in the separated region on the Coanda surface. The surface pressures calculated with the SARC and $k-\zeta$ models exhibit essentially the same behavior and agree reasonably well with the measured pressures. Since the predicted suction peaks are higher than the experimental ones, the computed C_L exceeds the experimental value by 15 percent. The influence of mesh density on the pressures computed with the SA model are shown in Figure 2b. There are only minor differences between the results, which include the solution obtained with FUN2D.

As evident in Fig. 2 there is an oscillation in the computed pressures on the upper part of the Coanda surface. This oscillatory behavior can also be seen in the surface skin-friction distribution depicted in Fig. 3, and it becomes more prominent with mesh refinement. Such behavior is a consequence of using measured coordinates for the definition of the airfoil geometry, since smoothness of the geometric slope and curvature are not guaranteed.

The streamlines on the aft section of the airfoil for the $C_\mu = 0.03$ experiment and for the fine grid computation with the SARC model are displayed in Fig. 4. These streamline patterns are similar. However, instead of the two distinct vortices that appear in the experiment at the lower part of the Coanda surface, there is one closed vortex and one hairpin vortex in the computation. The differences occur because the flow separates slightly sooner in the experiment than it does in the computation. For the experiment the jet detaches at 85 degrees around the Coanda surface, and for the calculation the jet departure takes place at approximately 90 degrees. Here, and in subsequent discussion, the angle (θ) is being referenced to the beginning of the circular trailing edge on the upper surface of the airfoil. In Figs. 5 - 8 the streamline patterns corresponding to the other turbulence models are shown. There are only minor differences between the streamlines for the $k-\zeta$ and SARC models, since the flow separates at approximately the same location. On the medium grid the vortical structure with the SST model is strikingly different than that with the other models. However, as seen in Fig. 8, a similar structure appears with refinement of the mesh. Thus, there is mesh sensitivity for the SST model that does not occur with the other models. As a result of the mesh refinement, the surface pressures in the separation region obtained with the SST model essentially coincide with those determined with the SA model.

To provide some indication of convergence behavior of the computations, the variation with multigrid cycles in the L_2 norm of the residual (for density equation) is presented in Fig. 9. Roughly 2300 cycles are required to reduce the residual four orders of magnitude. A contributing factor to this slow convergence is the slowly converging plenum solution, which is a consequence of the very low-speed flow in the plenum. The

implementation of low-speed preconditioning,[23-25] especially in the plenum, has the potential to provide a significant acceleration of convergence. By applying preconditioning to the particular case considered here, where $C_\mu = 0.03$, the number of cycles required to attain the same level of convergence obtained previously is reduced by almost a factor of two. However, we have not been able to attain this same improvement in convergence as the value of C_μ is increased. The benefit of low-speed preconditioning is apparently not maintained when there is an embedded region where the Mach number is significantly higher than the free-stream Mach number. An alternative approach to low-speed preconditioning is given by Rossow.[26]

As indicated previously the structured grid does not have the necessary resolution for the viscous layer adjacent to the trailing edge of the lip of the jet slot. In order to determine the effect of this on the velocity field, we now compare CFL3D solutions with those computed on the unstructured grid with FUN2D, using the SA model. Figure 10 shows a close-up of the vortical flow behind the vertical lip edge that is captured on the high definition unstructured grid. The velocity profiles from the FUN2D and CFL3D calculations are compared in Figs. 11 - 15. The most significant difference between the profiles occurs at the jet exit ($\theta = 0$ degrees), where there is reverse flow on the unstructured grid. On the Coanda surface there are minor differences at the knee of each profile, resulting from the resolution disparities. There is good agreement with the data except on the lower surface of the airfoil. In summary, the effect of not resolving the viscous layer on the blunt jet slot lip is almost totally local to the lip; downstream computed results are nearly the same. The effect of medium versus fine structured grid is also shown in these figures to be very minor, indicating reasonable resolution using the medium grid level.

Since fairly good agreement with the pressure data was obtained with the SARC model, the velocity and shear stress profiles computed with this model and the corresponding measured data are presented in Figs. 16a - 16c and Figs. 17a - 17c, respectively. There is a significant discrepancy between the predicted and experimental velocity profiles at the $\theta = 90$ degrees location due to the slightly earlier separation occurring in the experiment. For the Reynolds stress profiles there is fair agreement with the experimental data except in the vicinity of jet detachment.

Since a numerical method for CC airfoil flows must be able to provide solutions for a range of conditions, we now continue the evaluation of the present method by considering higher values of the jet momentum coefficient. In Fig. 18 the computed surface pressure variations for $C_\mu = 0.10$ are compared with experimental data. The relative agreement with the data and the trends discussed for the $C_\mu = 0.03$ case are similar here. Moreover, the pressures computed with the SARC model are the closest to the experiment, again confirming the importance of representing the curvature effects, which produce additional strain rate effects. Figures 18 and 19 show the influence of mesh density on the solution obtained with the SARC model. Surface pressures on the two meshes are nearly the same, and the skin friction distributions are fairly close on the Coanda surface.

The streamlines from the fine grid calculation with the SARC model are compared with those for the experiment in Fig. 20. In the experiment the flow separates at the angular location $\theta \approx 115$ degrees. For the computed flow separation occurs at θ of about 113 degrees. There is good agreement with the experimental streamlines. Although not perceptible in the figure, there is an extremely thin separation region on the lower surface of the airfoil near the trailing edge. This situation also exists for the $k - \zeta$ model solution shown in Fig. 21a. Such a recirculation zone would not have been detectable in the experiment. With the SA model there is a conspicuous separation bubble near the trailing edge, as shown in Fig. 21b. For the SST model the streamlines are displayed in Fig. 22. They exhibit a highly nonphysical behavior, forming a large vortex below the lower surface of the airfoil. The jet flow travels forward on the lower surface to near the $x/c = 0.25$ location before it turns and proceeds downstream. Steady-state convergence was not attained for this calculation, with the lift coefficient oscillating between 3.5 and 4.5. Thus, the streamlines in Fig. 22 only characterize the solution during the oscillation. The SST model does not include curvature effects; and perhaps, incorporating these effects would eliminate this nonphysical behavior (see Mani et al.[27] for curvature corrections for this SST model).

To further explain the effect of the turbulence modeling we examine turbulent viscosity profiles at two locations on the Coanda surface. As seen in Fig. 23 the turbulent viscosities determined with the SARC and

$k-\zeta$ models are larger those obtained with the SA model in the shear layer between the jet and the exterior flow. Thus, there is less entrainment of the lower speed exterior flow with the SA model, resulting in higher jet velocities. Near the surface the turbulent viscosities are larger when applying the SA model, which means that there is more higher momentum fluid being transported to the interior of the surface boundary layer. Both of these effects produce the delayed flow separation exhibited with the SA model.

In Figs. 24a - 24c the velocity profiles computed with the CFL3D and FUN2D codes are compared. Again, as in the $C_\mu = 0.03$ case, there are generally minor differences between the computed profiles. Unlike the $C_\mu = 0.03$ case there is a large disagreement with the experimental data at the $x/c = 0.875$ locations on the upper surface of the airfoil. An estimate of the velocity at the edge of the boundary layer based on static and total pressures is not consistent with the measured data. At this point we cannot account for the lower velocities of the experiment.

In order to examine the physics of the flow over the CCW configuration and also the wind tunnel wall interference effects, we performed a preliminary three-dimensional (3-D) calculation. With this simulation we accounted for the wind tunnel blockage effects as well as sidewall boundary-layer effects. There was no angle of attack correction employed in the 3-D simulation. Figure 25 displays the streamlines of the 3-D simulation, and one clearly sees the vortical structures due to the circulation control and interaction with the sidewalls. Although not shown, the 3-D pressure distribution using the SST model is similar to many of the 2-D results shown earlier. This preliminary result further substantiates the angle of attack corrections provided by the experimenters. In addition, the 3-D prediction of the velocity profile at $x/c = 0.875$ is similar to the profiles of the 2-D calculations.

The velocity and shear stress profiles computed with the SARC model are given in Figs. 26a - 26c and Figs. 27a - 27c, respectively. At the $\theta = 30$ degrees location the effect of the discrepancy with the experimental velocity profile at $x/c = 0.875$ on the upper surface remains. In the neighborhood of separation, there is reasonable agreement with the measured profiles. Once again there is only fair agreement with the experimental Reynolds stress profiles.

In the first two cases ($C_\mu = 0.03$ and 0.10) the flow at the jet exit is subsonic. For the $C_\mu = 0.226$ case the flow at the jet exit is sonic. The Mach contours for the calculation with the SARC model are displayed in Fig. 28. Pressure distributions for this case (using SA and SARC models only) are presented in Fig. 29. On the suction surface the pressures computed with the SARC model are lower than the measured ones, resulting in a lift coefficient that is 29 percent higher than the experimental value. The streamlines for this solution are shown in Fig. 30. Although the pressures corresponding to the SA model at first glance appear to agree well with experiment, the SA results are actually very poor: the streamlines exhibit a nonphysical jet wraparound behavior, which is depicted in Fig. 31. Although not shown, the solutions with both the SST and $k-\zeta$ models also exhibit nonphysical jet behavior for this case.

The variation of the lift coefficient C_L with the jet momentum coefficient C_μ is presented in Fig. 32. Since the SARC model performed the best in modeling the Coanda-flow physics, only the results with the SARC model are shown. Figure 32 demonstrates that even though the computed results agree fairly well with the experiment at the lower C_μ, they still significantly overpredict the lift coefficient at higher C_μ. Such a discrepancy in C_L can be caused by delayed separation and/or overprediction of the pressure suction peaks. The lift coefficients for the medium and fine grids are given in Table 2.

Concluding Remarks

Three low Mach number CC airfoil flows have been computed. With these three cases both low and high values for the jet momentun coefficient have been considered. Several transport equation models for turbulence have been investigated. These models include the one-equation SA model, the SA model with curvature correction (SARC), the SST model of Menter, and the k-enstrophy model ($k-\zeta$). Comparisons have been made with surface pressures, velocity profiles, Reynolds stress profiles, and streamline patterns form the Novak et al. experiment. The effect of mesh density on the solutions has been examined. Results with the structured grid code CFL3D have been compared to those obtained with the unstructured code FUN2D.

Model	C_μ	Grid	$(C_L)_{exp}$	C_L	C_D
SA	0.030	med.	1.500	1.916	0.02656
	0.030	fine		1.922	0.02472
SA	0.105	med.	3.575	4.692	0.06347
	0.105	fine		4.761	0.05312
SARC	0.030	med.	1.500	1.725	0.02493
	0.030	fine		1.741	0.02329
SARC	0.105	med.	3.575	3.940	0.04736
	0.105	fine		4.045	0.04449
SARC	0.226	med.	5.452	6.674	0.1209
	0.226	fine		7.046	0.1257
SST	0.030	med.	1.500	1.943	0.03283
	0.030	fine		1.921	0.02510
$k-\zeta$	0.030	med.	1.500	1.739	0.02922
$k-\zeta$	0.105	med.	3.575	4.214	0.06237

Table 2. Comparison of computed and experimental lift coefficients for circulation control airfoil.

A highly clustered grid in the neighborhood of the jet exit has been used in the FUN2D computations. With the exception of velocity profiles at the jet exit, the CFL3D and FUN2D codes produce almost the same results using the SA turbulence model.

The importance of including curvature effects when computing CC airfoil flows has been demonstrated. For all three CC airfoil flow cases the closest agreement with the experimental surface pressures and streamlines has been computed with the SARC model. However, as the jet velocity is increased, the numerical solution deteriorates, generally delaying separation and resulting in a lift coefficient that exceeds the experimental value. The reason for this deterioration is not understood.

For the two jet momentum coefficients $C_\mu = 0.03$ and $C_\mu = 0.10$, the $k-\zeta$ model performs similar to the SARC model, whereas the SA and SST models produce significantly greater delay in separation. The reason why the $k-\zeta$ model performs better for these cases than the SA and SST models is not known at this time. For $C_\mu = 0.226$ the jet predicted with the SA, SST, and $k-\zeta$ models wraps unphysically far around the airfoil. Among the models tested, only the SARC model produces physically realistic solutions at the highest blowing rate.

References

[1]Anders, S. G, Sellers, W. L., Washburn, A. E., "Active Flow Control Activities at NASA Langley," *AIAA Paper* 04-2623, 2004.

[2]Jones, G. S., and Englar, R. J, "Advances in Pneumatic-Controlled High-Lift Systems Through Pulsed Blowing," *AIAA Paper* 03-3411, 2003.

[3]Jones, G. S., and Joslin, R. D (editors), Proceedings of Circulation Control Workshop, NASA CP 2005-213509, Hampton, Virginia, March 2004.

[4]Abramson, J., "Two-Dimensional Subsonic Wind Tunnel Evaluation of Two Related Cambered 15-Percent Circulation Control Airfoils," DTNSRDC ASED-373, 1977.

[5]Swanson, R. C., Rumsey, C. L, Anders, S. G., "Aspects of Numerical Simulation of Circulation Control Airfoils," Proceedings of Circulation Control Workshop, NASA CP 2005-213509, Hampton, Virginia, March 2004.

[6]Krist, S. L., Biedron R. T. and Rumsey, C. L., "CFL3D User's Manual," *NASA TM* 1998-208444, 1998.

[7]Abramson, J., and Rogers, E., "High-Speed Characteristics of Circulation Control Airfoils," *AIAA Paper* 83-0265, 1983.

[8]Spalart, P. R. and Shur, M., "On the Sensitization of Turbulence Models to Rotation and Curvature," *Aerospace Sci. Technol.*, vol. 5, pp. 297–302, 1997.

[9]Menter, F. R., "Improved Two-Equation $k-\omega$ Turbulence Model for Aerodynamic Flows," *NASA TM* 103975, 1992.

[10]Novak, C. J., Cornelius, K. C, Roads, R. K., "Experimental Investigations of the Circular Wall Jet on a Circulation Control Airfoil," *AIAA Paper* 87-0155, 1987.

[11]Novak, C. J., and Cornelius, "An LDV Investigation of a Circulation Control Airfoil," *AIAA Paper* 86-0503, 1986.

[12]Shrewsbury, G. D., "Numerical Evaluation of Circulation Control Airfoil Performance Using Navier-Stokes Methods," *AIAA Paper* 86-0286, 1986.

[13]Shrewsbury, G. D., "Numerical Study of a Research Circulation Control Airfoil Using Navier-Stokes Methods," *J. Aircraft*, vol. 26, No. 1, pp. 29–34, 1989.

[14]Viegas, J. R., Rubesin, M. W., MacCormack, R. W, "On the Validation of a Code and a Turbulence Model Appropriate for Circulation Control Airfoils," AGARD, Validation of Computational Fluid Dynamics, Volume 1: Symposium Papers and Round Table Discussion, 1988.

[15]Baldwin, B. S., and Lomax, H., "Thin Layer Approximation and Algebraic Model for Separated Flows," *AIAA Paper* 78-257, 1978.

[16]Roe, P., "Approximate Riemann Solvers, Parameter Vectors, and Difference Schemes," *J. of Comp. Phys.*, vol. 43, pp. 357–372, 1981.

[17]Anderson, W. K., and Bonhaus, D. L., "An Implicit Upwind Algorithm for Computing Turbulent Flows on Unstructured Grids," *Computers & Fluids.*, vol. 23, no. 1, pp. 1–21, 1994.

[18]Spalart, P. R. and Allmaras, S. R., "A One-Equation Turbulence Model for Aerodynamic Flows," *La Recherche Aerospatiale*, vol. 1, pp. 5–21, 1994.

[19]Rumsey, C. L., Gatski, T. B., Anderson, W. K. and Nielsen, E. J., "Isolating Curvature Effects in Computing Wall-Bounded Turbulent Flows," *Inter. J. of Heat and Fluid Flow*, vol. 22, pp. 573–582, 2001.

[20]Menter, F. R., "Zonal Two Equation $k-\omega$ Turbulence Model for Aerodynamic Flows," *AIAA Paper* 93-2906, 1993.

[21]Menter, F. R., "Two-Equation Eddy-Viscosity Turbulence Models for Engineering Applications," *AIAA J.* vol. 32, No. 8, pp. 1598–1605, 1994.

[22]Robinson, D. F., and Hassan, H. A., "Further Development of the $k-\zeta$ (Enstropy) Turbulence Closure Model," *AIAA J.*, vol. 36, No. 10, pp. 1825–1833, 1998.

[23]Turkel, T., Vatsa, V. N. and Radespiel, R., "Preconditioning Methods for Low-Speed Flow," *AIAA* , 96-2460, 1996.

[24]Turkel, T., Radespiel, R. and Kroll, N., "Assessment of Two Preconditioning Methods for Aerodynamic Problems," *Computers & Fluids*, vol. 26, no. 6, pp. 613–634, 1997.

[25]Turkel, T., "Preconditioning Techniques in Computational Fluid Dynamics," *Annual Review of Fluid Mechanics*, vol. 31, pp. 385–416, 1999.

[26]Rossow, C.-C., "Extension of a Compressible Code Towards the Incompressible Limit," *AIAA Paper* 03-432, 2003.

[27]Mani, M., Ladd, J. A. and Bower, W. W., "Rotation and Curvature Assessment for One- and Two-Equation Turbulence Models," *J. Aircraft*, vol. 41, No. 2, pp. 268–273, 2004.

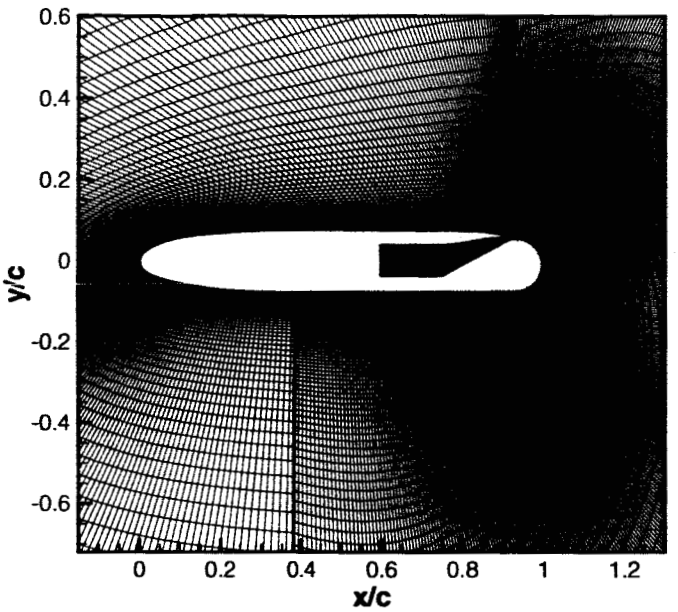

Figure 1a. Partial view of fine structured grid.

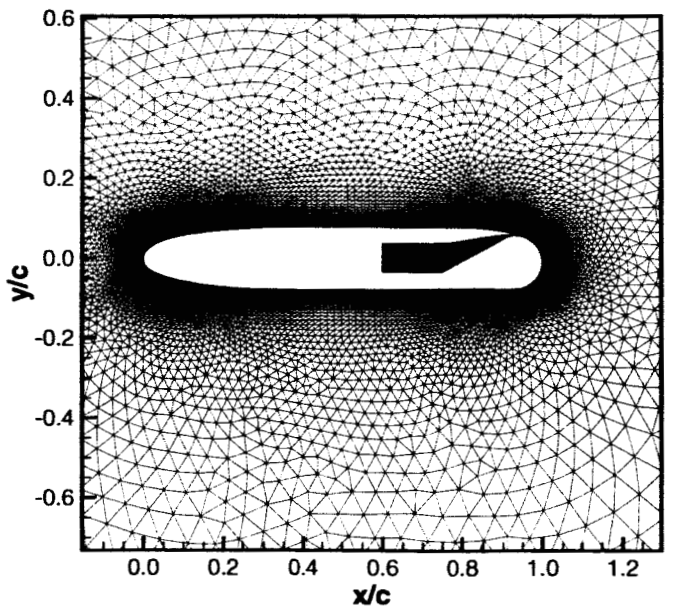

Figure 1b. Partial view of unstructured grid.

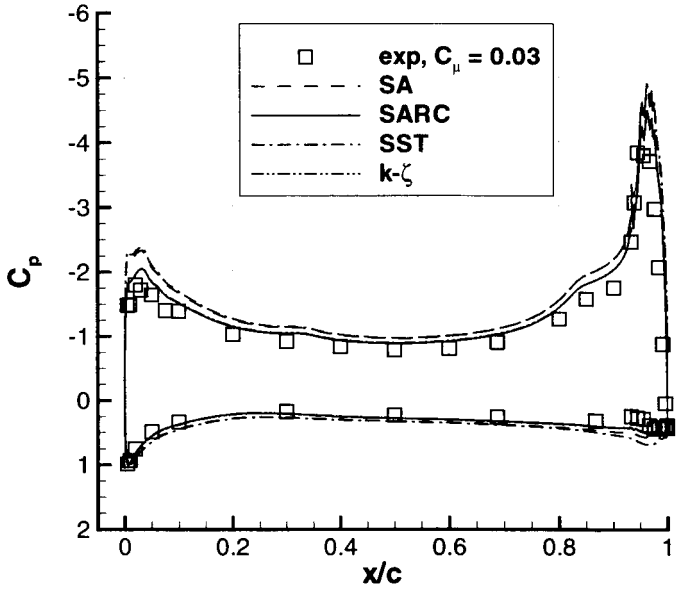

(a) SA, SARC, SST, $k-\zeta$ models, CFL3D, medium grid

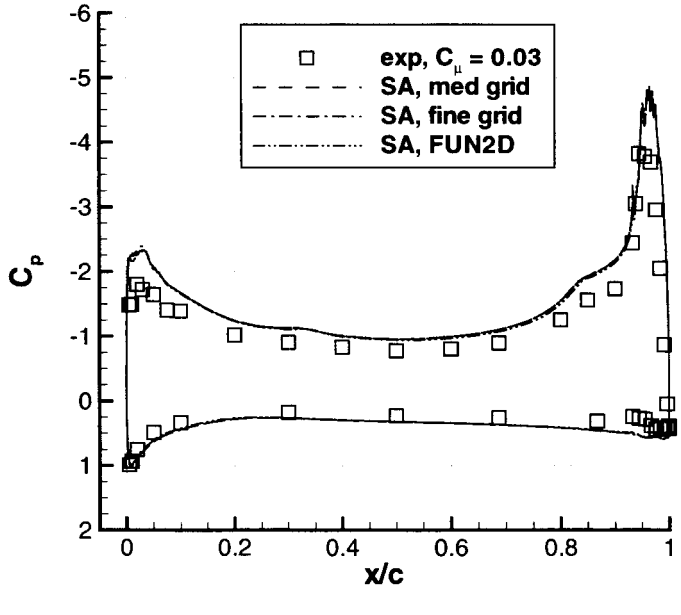

(b) SA model, CFL3D and FUN2D

Figure 2. Comparison of surface pressures computed with several turbulence models ($M_\infty = 0.12$, $\alpha = -2.46°$, $Re_c = 0.986 \times 10^6$, $C_\mu = 0.03$).

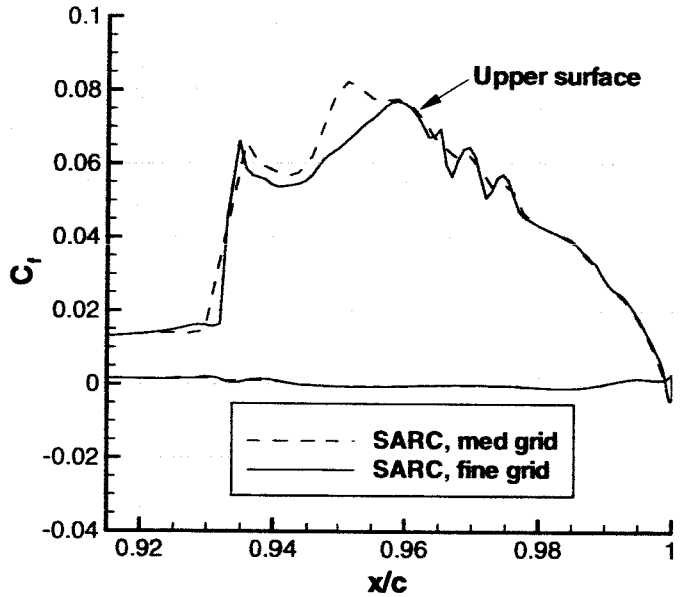

Figure 3. Surface skin friction computed with SARC model ($M_\infty = 0.12$, $\alpha = -2.46°$, $Re_c = 0.986 \times 10^6$, $C_\mu = 0.03$).

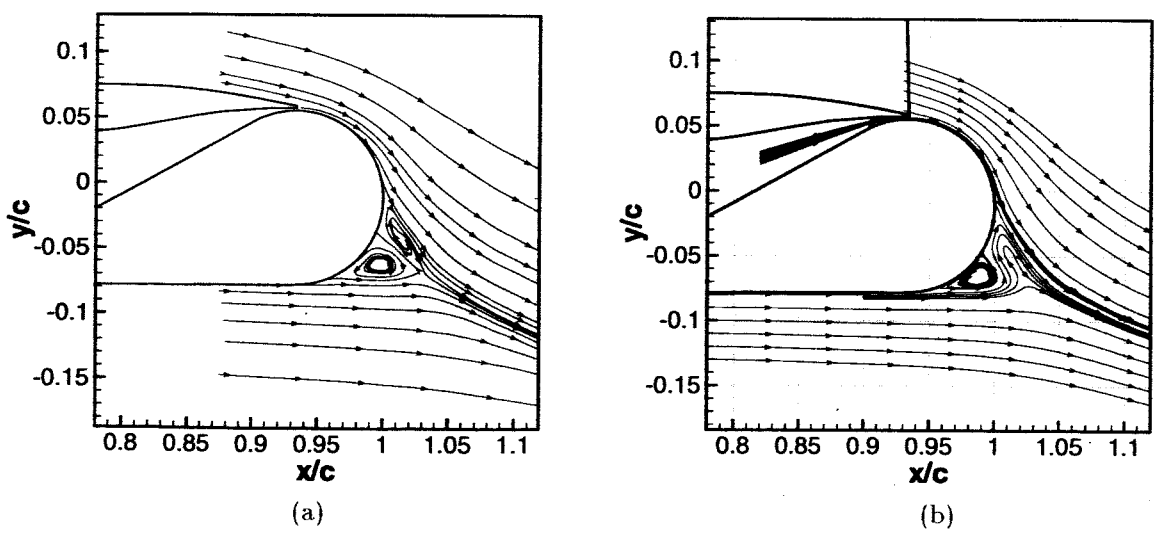

Figure 4. Streamlines, $C_\mu = 0.03$: (a) experiment, (b) computation, SARC model, medium grid.

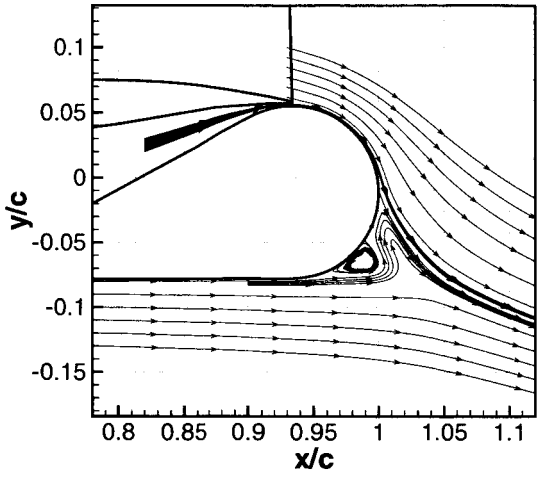

Figure 5. Streamlines, $C_\mu = 0.03$, $k-\zeta$ model, medium grid.

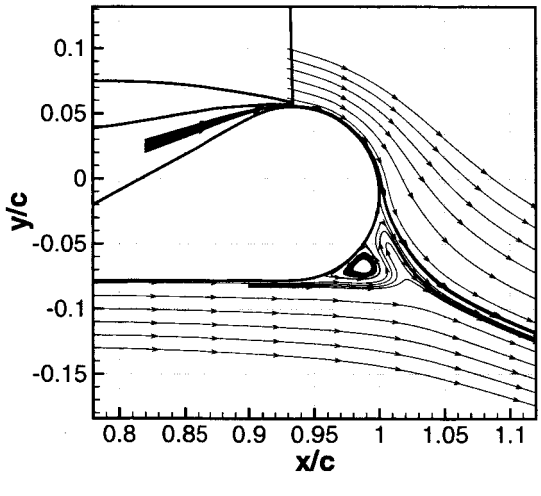

Figure 6. Streamlines, $C_\mu = 0.03$, SA model, medium grid.

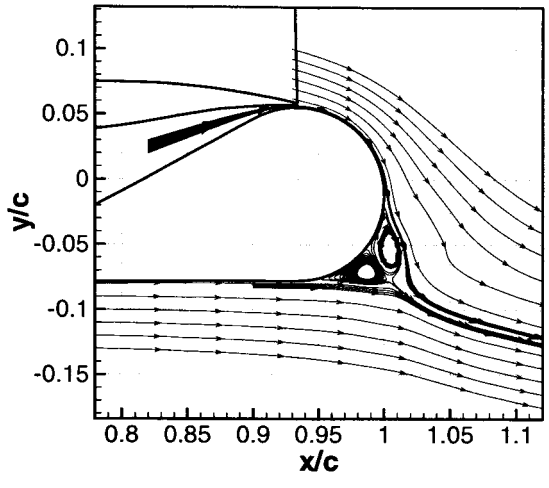

Figure 7. Streamlines, $C_\mu = 0.03$, SST model, medium grid.

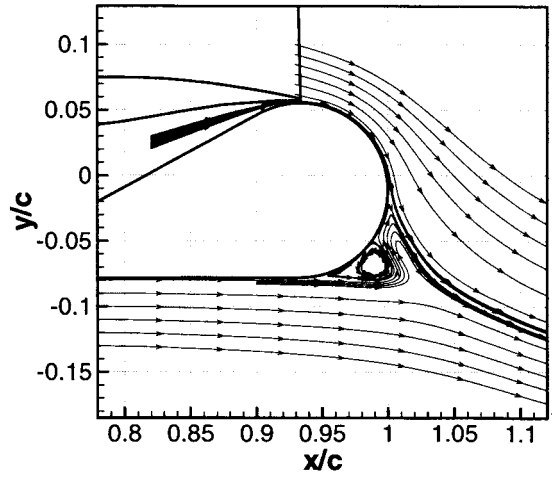

Figure 8. Streamlines, $C_\mu = 0.03$, SST model, fine grid.

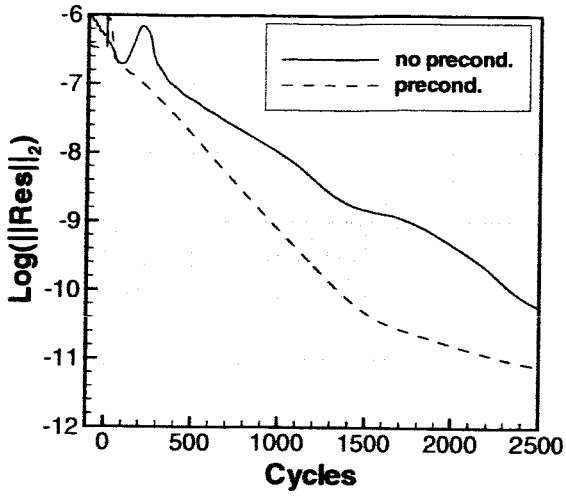

Figure 9. Residual histories with SA model, $C_\mu = 0.03$.

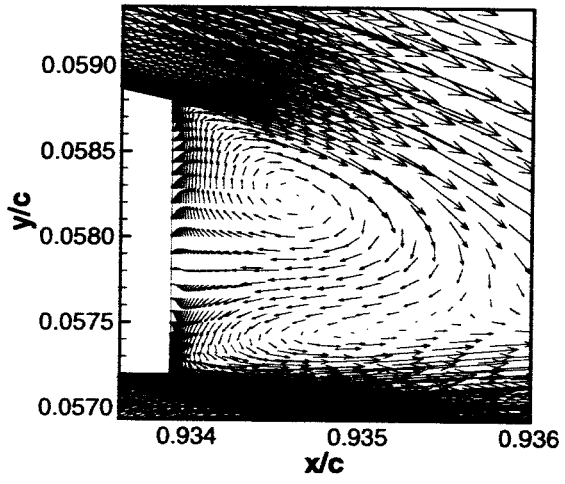

Figure 10. Velocity vectors, $C_\mu = 0.03$, SA model, FUN2D.

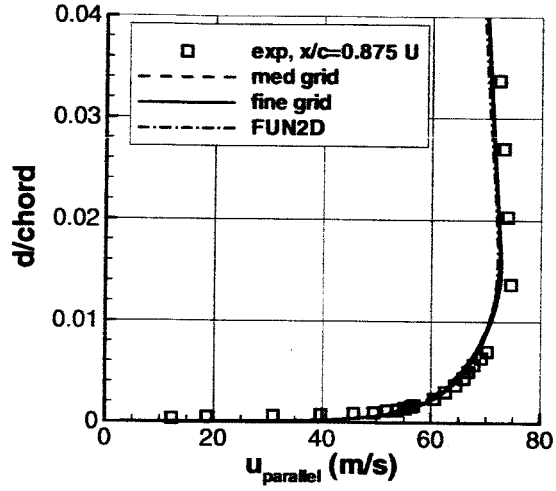

Figure 11. Velocity profiles, $C_\mu = 0.03$, SA model, $x/c = 0.875U$.

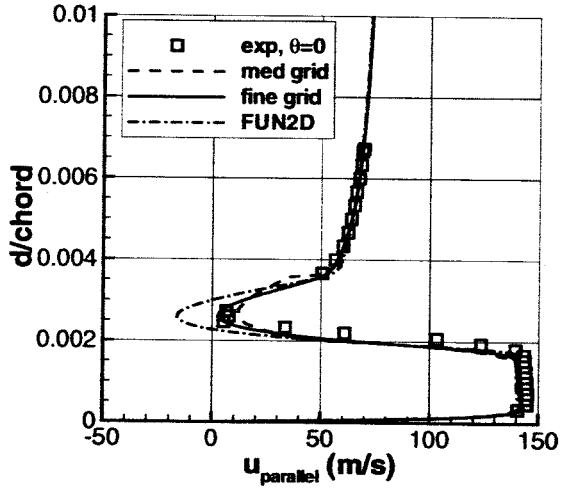

Figure 12. Velocity profiles, $C_\mu = 0.03$, SA model, $\theta = 0$ degrees.

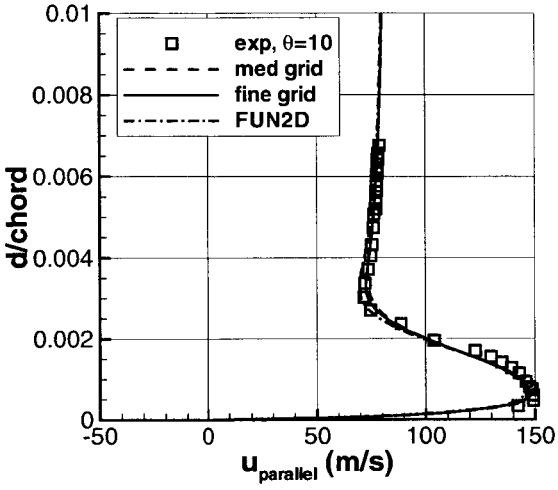

Figure 13. Velocity profiles, $C_\mu = 0.03$, **SA** model, $\theta = 10$ degrees.

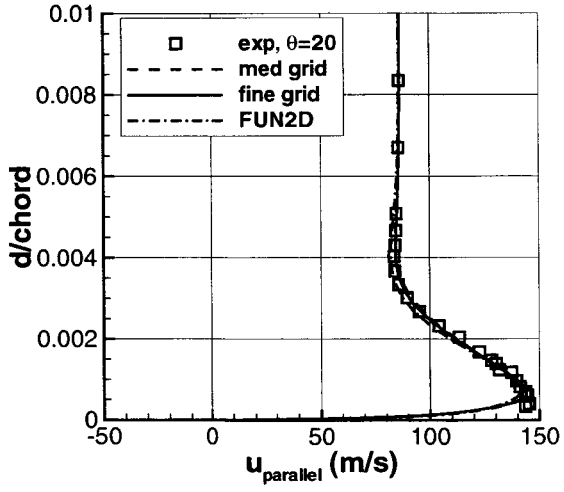

Figure 14. Velocity profiles, $C_\mu = 0.03$, **SA** model, $\theta = 20$ degrees.

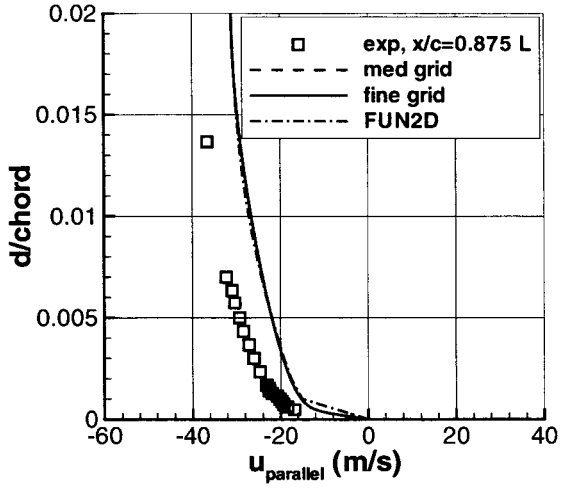

Figure 15. Velocity profiles, $C_\mu = 0.03$, **SA** model, $x/c = 0.875$**L**.

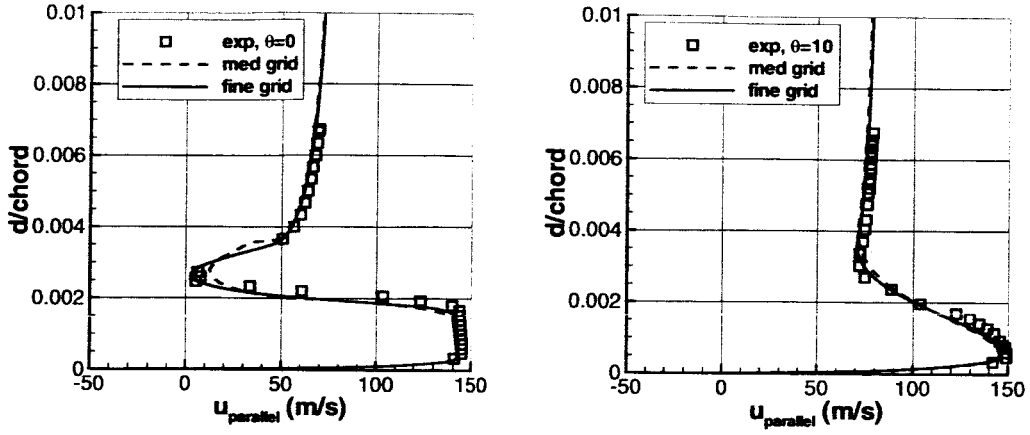

Figure 16a. Velocity profiles, $C_\mu = 0.03$, CFL3D, SARC model, $\theta = 0, 10$ degrees.

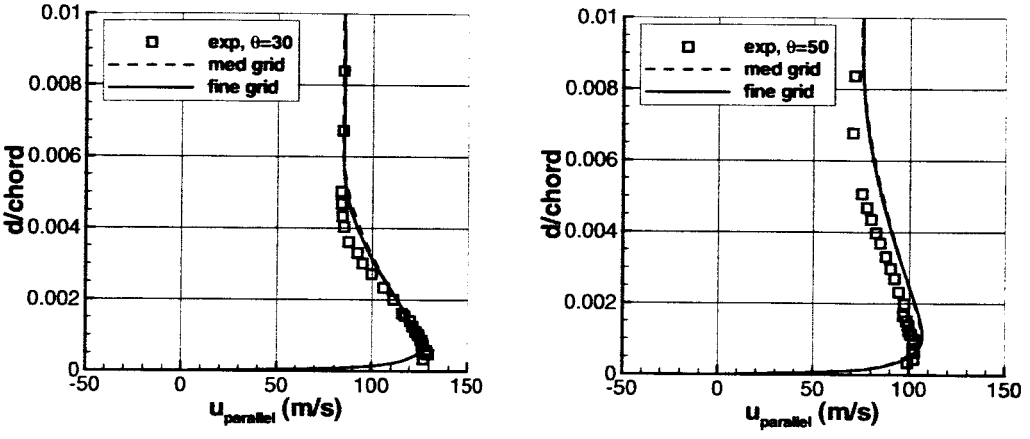

Figure 16b. Velocity profiles, $C_\mu = 0.03$, CFL3D, SARC model, $\theta = 30, 50$ degrees.

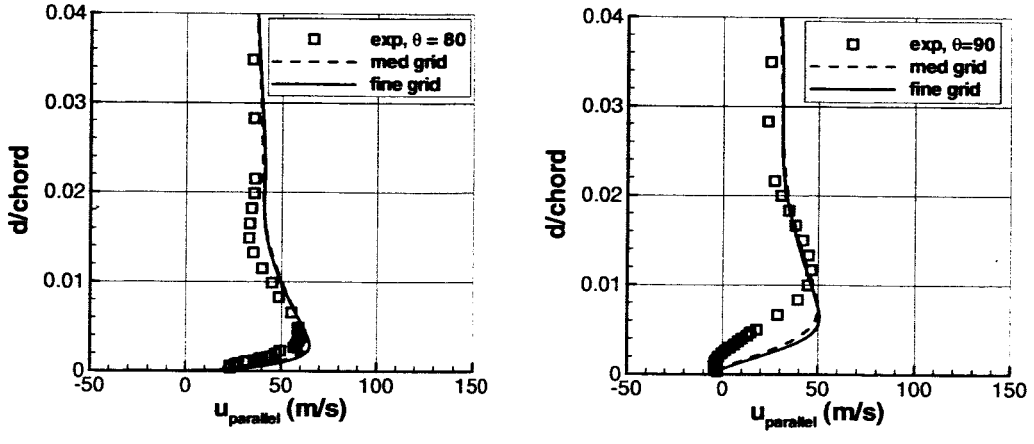

Figure 16c. Velocity profiles, $C_\mu = 0.03$, CFL3D, SARC model, $\theta = 80, 90$ degrees.

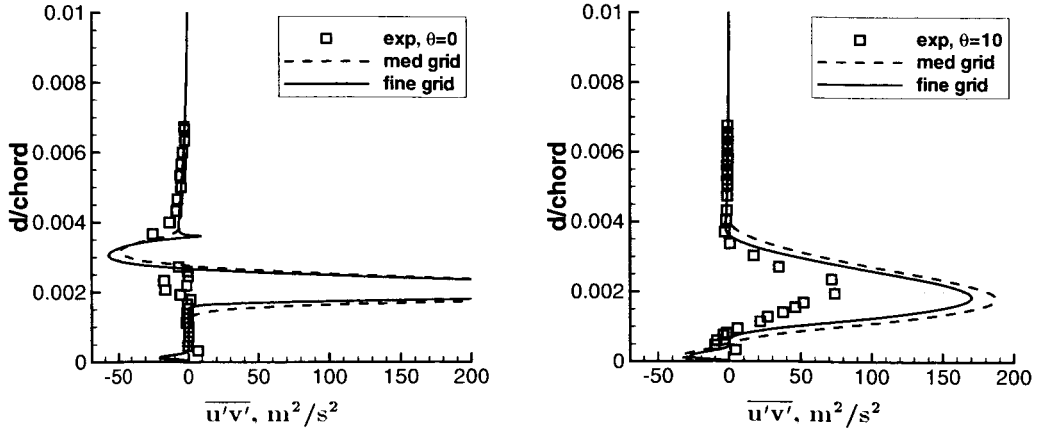

Figure 17a. Shear stress profiles, $C_\mu = 0.03$, CFL3D, SARC model, $\theta = 0, 10$ degrees.

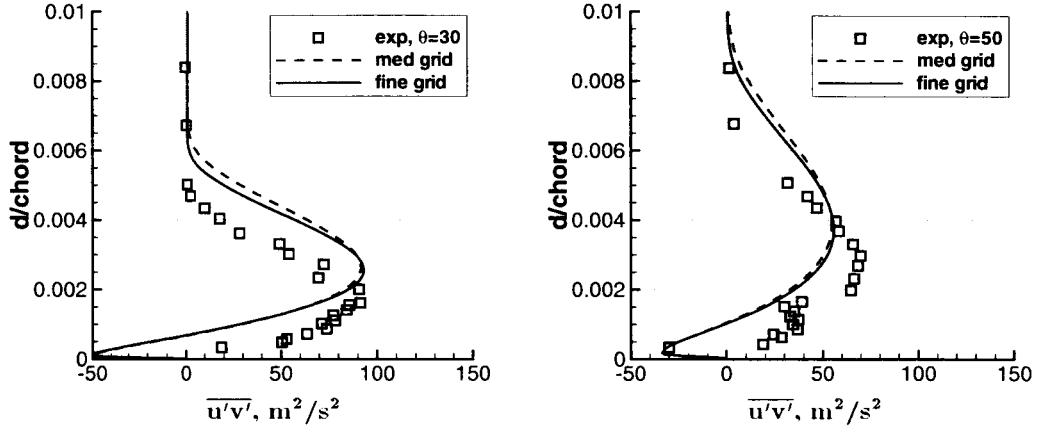

Figure 17b. Shear stress profiles, $C_\mu = 0.03$, CFL3D, SARC model, $\theta = 30, 50$ degrees.

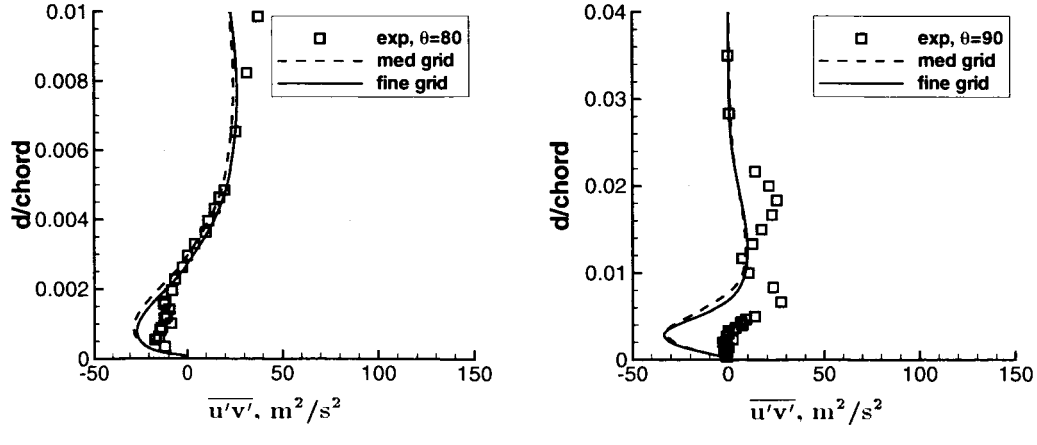

Figure 17c. Shear stress profiles, $C_\mu = 0.03$, CFL3D, SARC model, $\theta = 80, 90$ degrees.

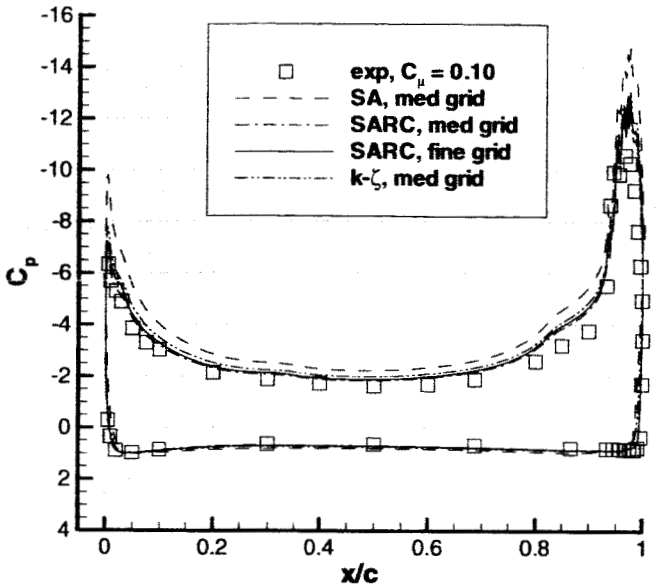

Figure 18. Surface pressures computed with several turbulence models ($M_\infty = 0.12$, $\alpha = -5.86°$, $Re_c = 0.986 \times 10^6$, $C_\mu = 0.10$).

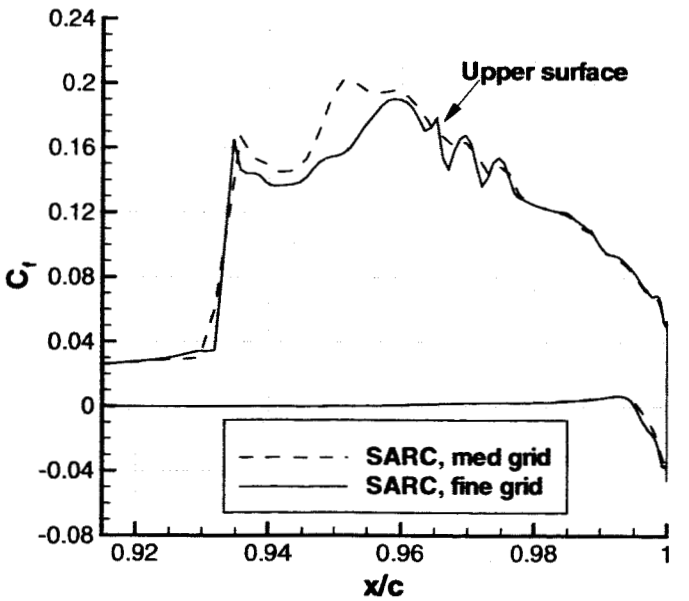

Figure 19. Surface skin friction computed with SARC model ($M_\infty = 0.12$, $\alpha = -5.86°$, $Re_c = 0.986 \times 10^6$, $C_\mu = 0.10$).

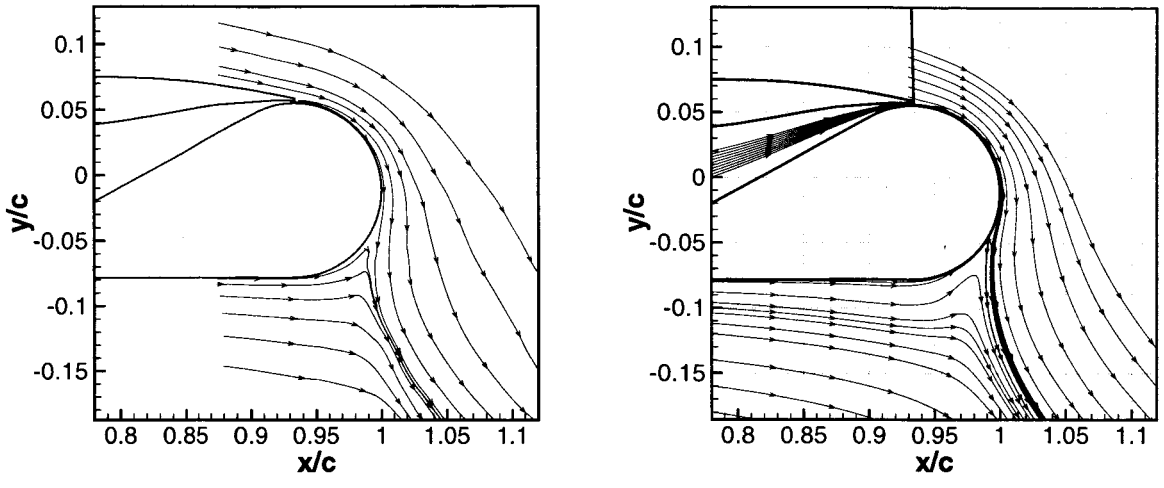

Figure 20. Streamlines, $C_\mu = 0.10$: (a) experiment, (b) computation, SARC model, fine grid.

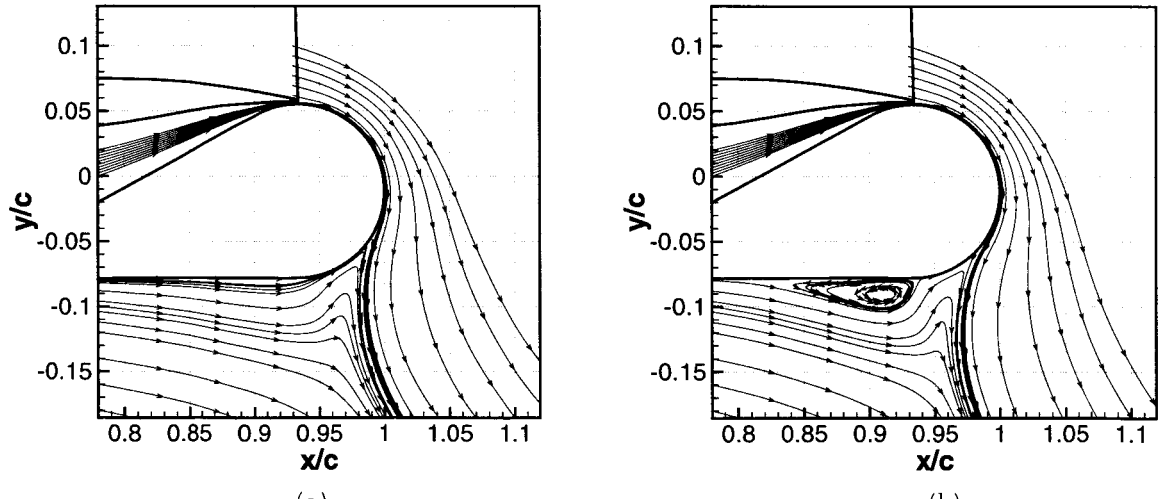

Figure 21. Streamlines, $C_\mu = 0.10$: (a) $k - \zeta$ model, medium grid (b) SA model, fine grid.

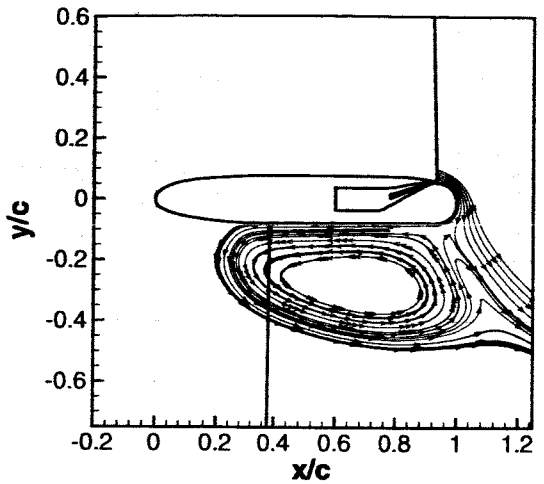

Figure 22. Streamlines, $C_\mu = 0.10$, SST model, medium grid.

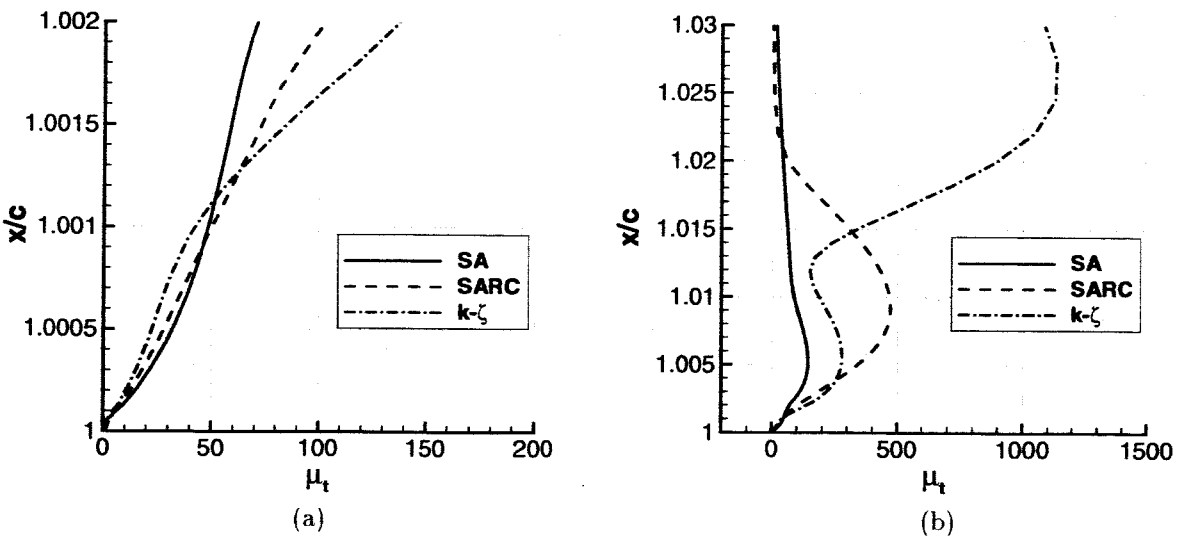

Figure 23. Turbulent viscosity, $C_\mu = 0.10$, $\theta = 90°$: (a) Near surface, (b) Outer region.

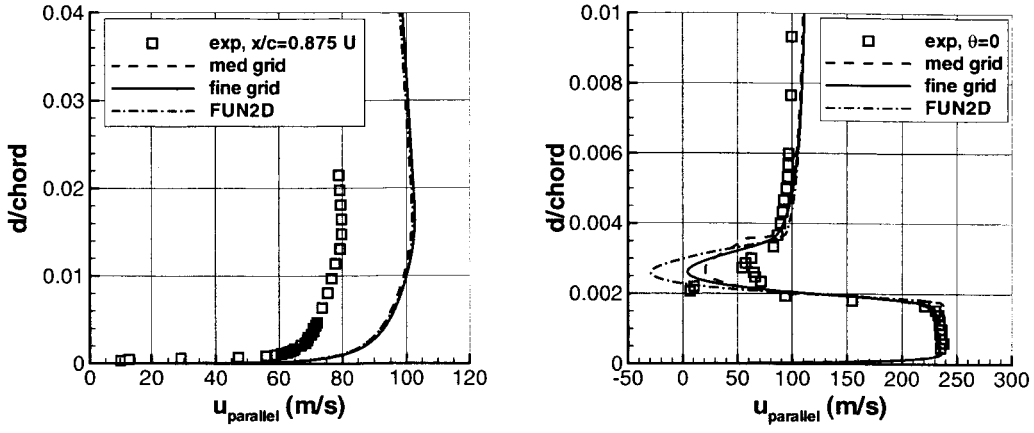

Figure 24a. Velocity profiles, $C_\mu = 0.10$, SA model, $x/c = 0.875U$ and $\theta = 0^o$.

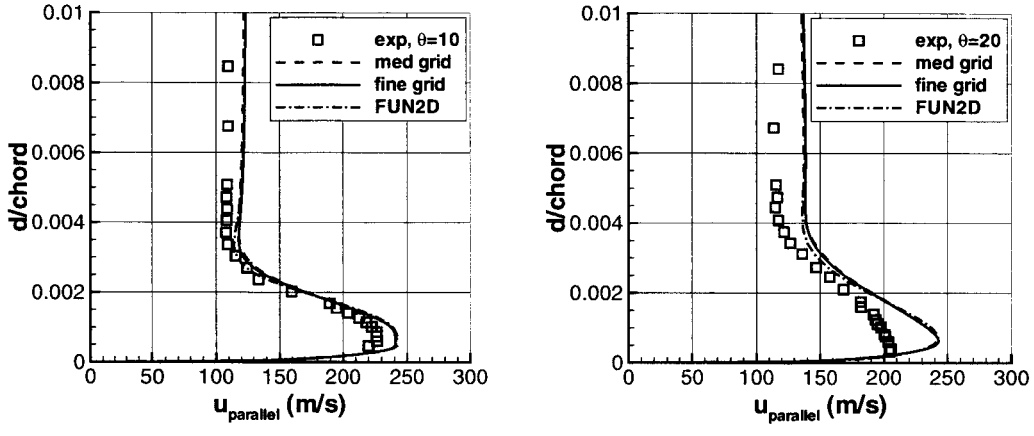

Figure 24b. Velocity profiles, $C_\mu = 0.10$, SA model, $\theta = 10, 20$ degrees.

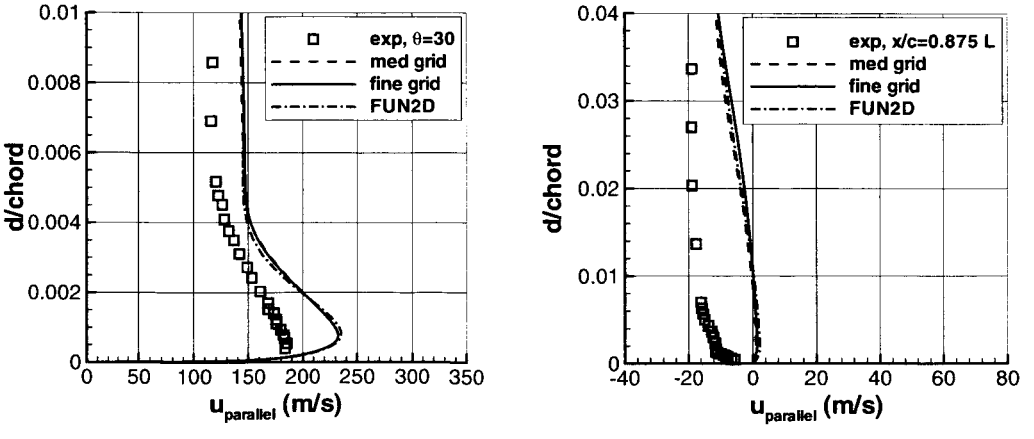

Figure 24c. Velocity profiles, $C_\mu = 0.10$, SA model, $\theta = 30^o$ and $x/c = 0.875L$.

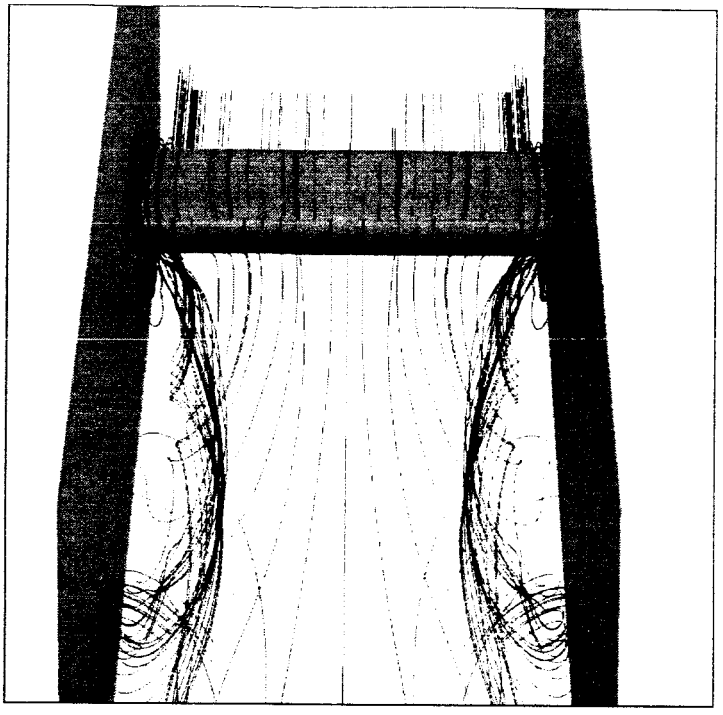

(a) Flow from top to bottom

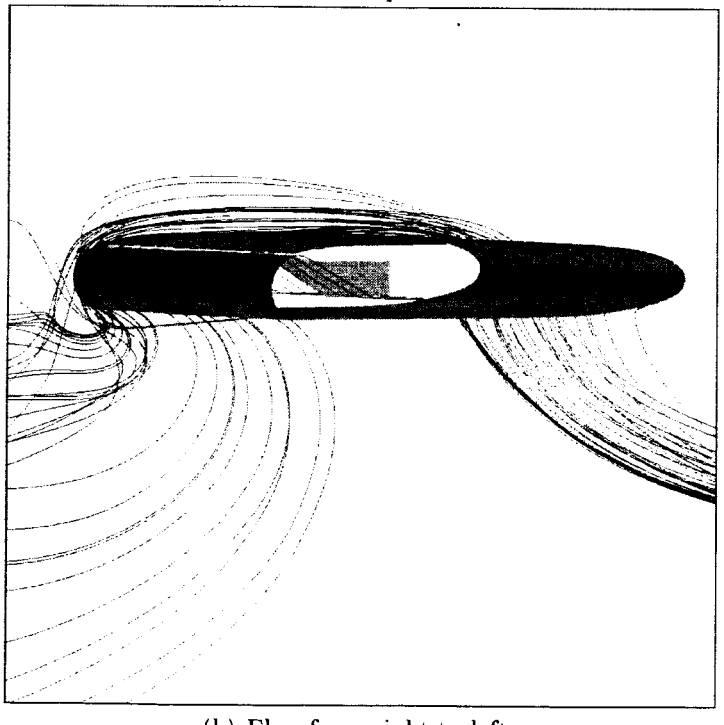

(b) Flow from right to left

Figure 25. Sreamlines for 3-D CFL3D calculation, SST, $C_\mu = 0.10$, fine grid.

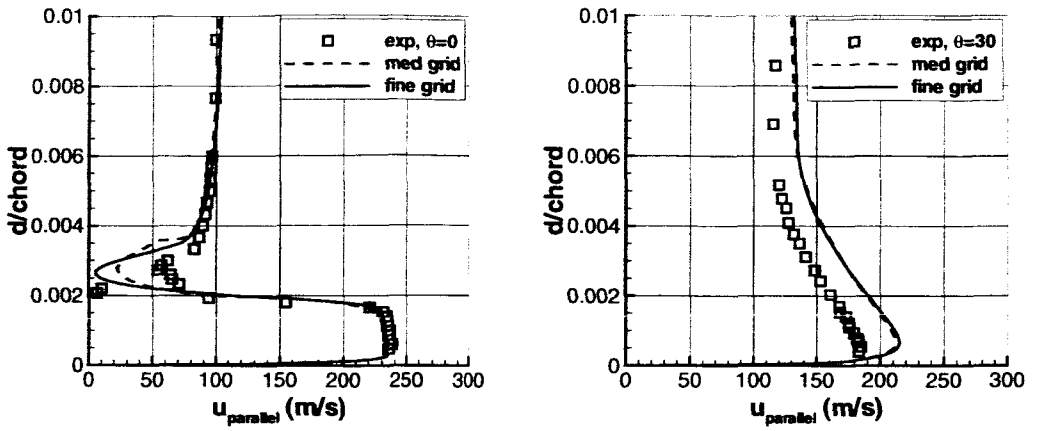

Figure 26a. Velocity profiles, $C_\mu = 0.10$, CFL3D, SARC model, $\theta = 0, 30$ degrees.

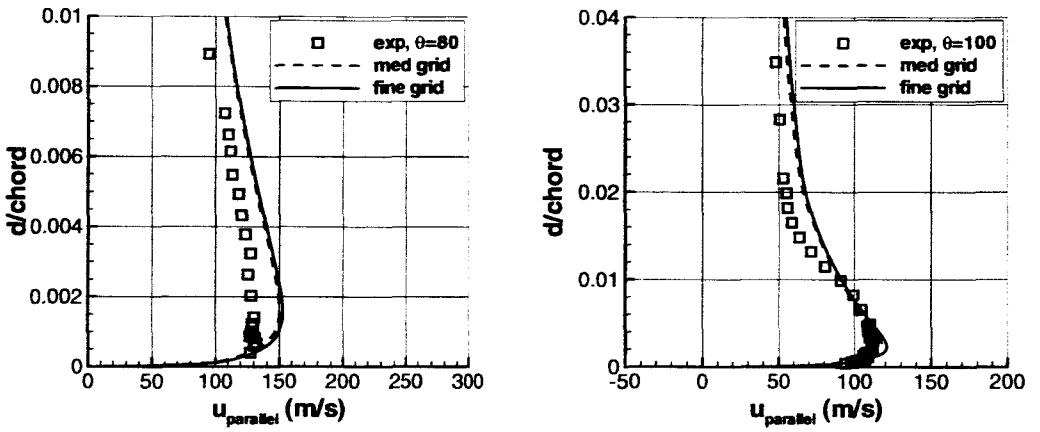

Figure 26b. Velocity profiles, $C_\mu = 0.10$, CFL3D, SARC model, $\theta = 30, 100$ degrees.

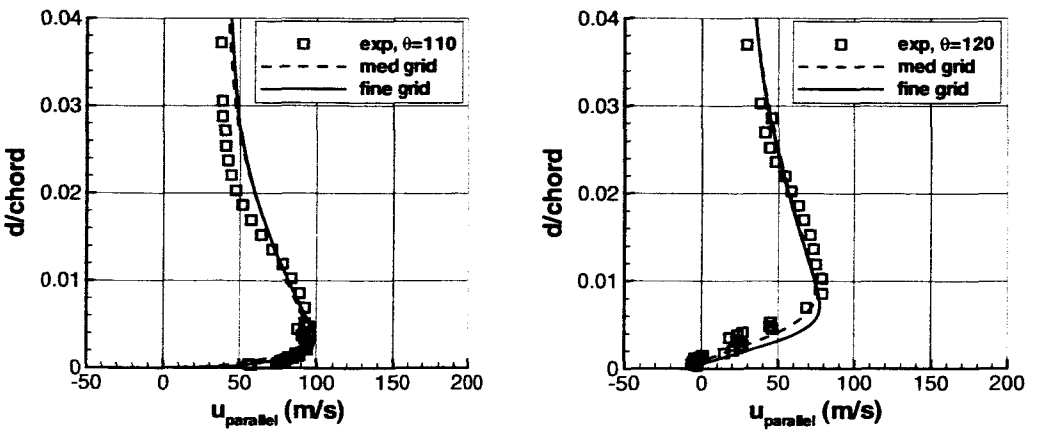

Figure 26c. Velocity profiles, $C_\mu = 0.10$, CFL3D, SARC model, $\theta = 110, 120$ degrees.

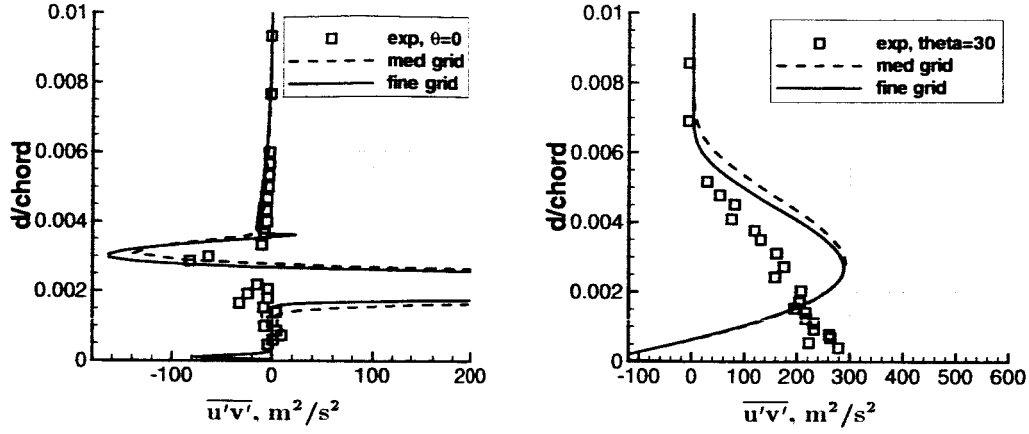

Figure 27a. Shear stress profiles, $C_\mu = 0.10$, CFL3D, SARC model, $\theta = 0.30$ degrees.

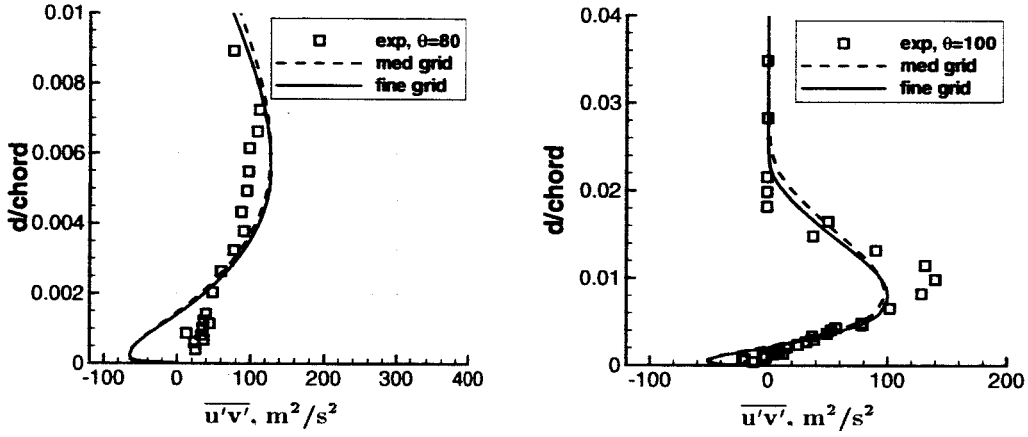

Figure 27b. Shear stress profiles, $C_\mu = 0.10$, CFL3D, SARC model, $\theta = 80, 100$ degrees.

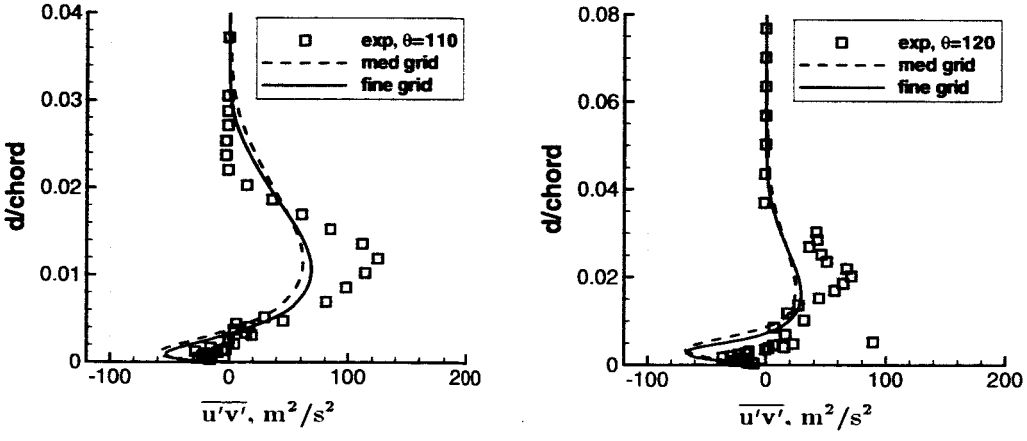

Figure 27c. Shear stress profiles, $C_\mu = 0.10$, CFL3D, SARC model, $\theta = 110, 120$ degrees.

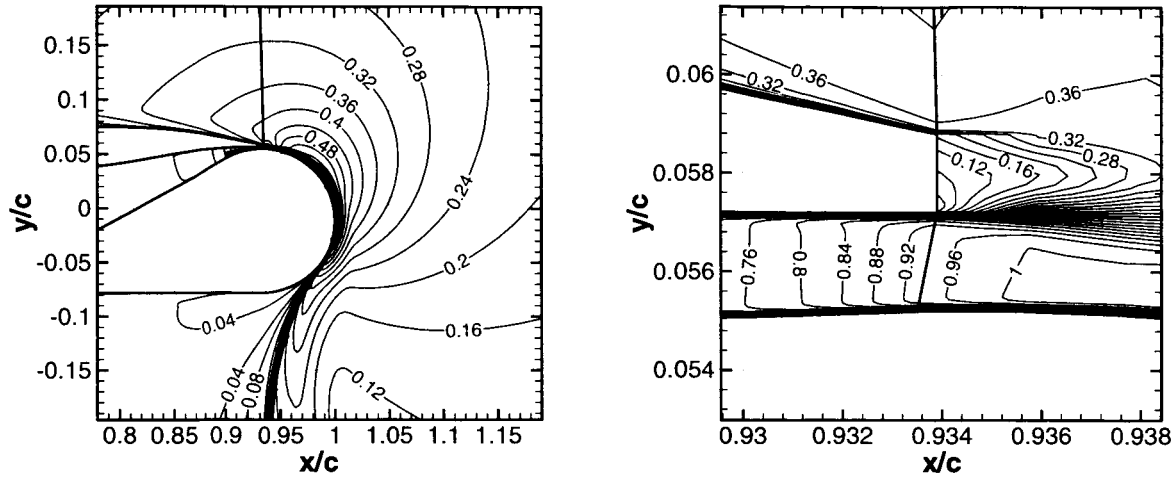

(a) (b)

Figure 28. Mach number contours, $C_\mu = 0.226$, SARC model: (a) trailing edge region, (b) vicinity of jet exit.

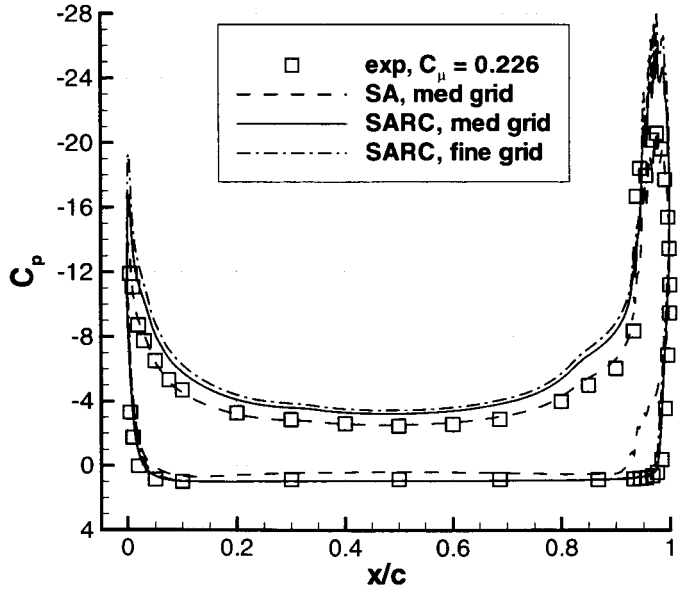

Figure 29. Comparison of surface pressures ($M_\infty = 0.12$, $\alpha = -8.94°$, $Re_c = 0.986 \times 10^6$, $C_\mu = 0.226$).

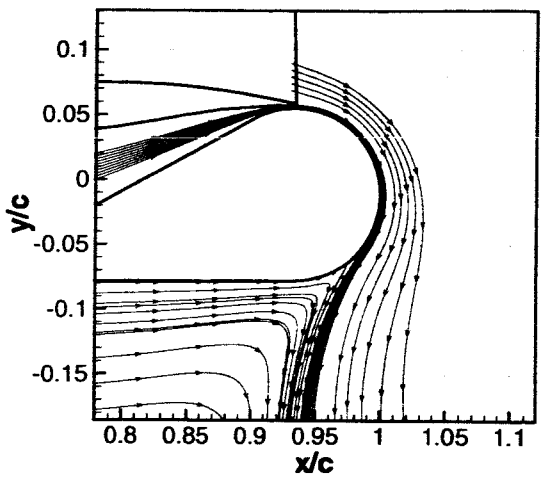

Figure 30. Streamlines with SARC model, $C_\mu = 0.226$, medium grid.

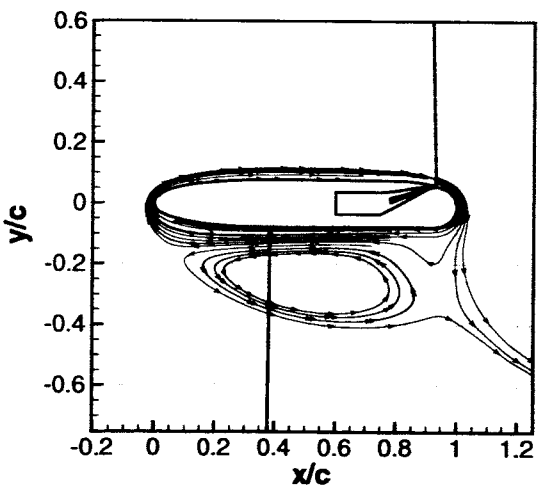

Figure 31. Streamlines with SA model, $C_\mu = 0.226$, medium grid.

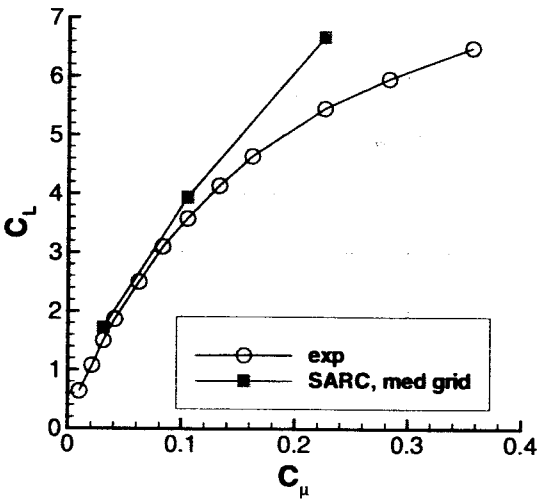

Figure 32. Variation of lift coefficient with jet momentum coefficient.